Chloride electrolyte enabled practical zinc metal battery with a near-unity Coulombic efficiency

Heng Jiang[1,2], Longteng Tang ®[1], Yanke Fu[3], Shitong Wang[4],
Sean K. Sandstrom ®[1], Alexis M. Scida[1], Guoxing Li[5], David Hoang[1],
Jessica J. Hong[1], Nan-Chieh Chiu[1], Kyriakos C. Stylianou ®[1],
William F. Stickle ®[6], Donghai Wang[5], Ju Li ®[4], P. Alex Greaney ®[3]✉,
Chong Fang ®[1]✉ & Xiulei Ji ®[1,2]✉

Rechargeable aqueous zinc batteries are finding their niche in stationary storage applications where safety, cost, scalability and carbon footprint matter most. However, harnessing this reversible two-electron redox chemistry is plagued by major technical issues, notably hydrogen evolution reaction (HER) at the zinc surface, whose impacts are often not revealed under typical measurement conditions. Here we report a concentrated electrolyte design that eliminates this parasitic reaction and enables a Coulombic efficiency (CE) of 99.95% for Zn plating/stripping measured at a low current density of 0.2 mA cm^{-2}. With extra chloride salts and dimethyl carbonate in concentrated $ZnCl_2$ electrolyte, the hybrid electrolyte with a unique chemical environment features low Hammett acidity and facilitates the in situ formation of a dual-layered solid electrolyte interphase, protecting zinc anodes from HER and dendrite growth. Benefiting from the near-unity CE, the pouch cell with a $VOPO_4 \cdot 2H_2O$ cathode sustains 500 deep cycles without swelling or leaking and delivers an energy density of 100 Wh kg^{-1} under practical conditions. Our work represents a critical step forward in accelerating the market adoption of zinc batteries as an energy storage system with higher sustainability.

The widespread commercialization of rechargeable aqueous zinc metal batteries (ZMBs) hinges on the sufficiently high Zn plating/stripping Coulombic efficiency (CE)[1–5]. The challenges of securing high CE of zinc metal anode (ZMA) stem from irreversible hydrogen evolution reaction (HER) across the life span and Zn dendrite formation during plating. Compared with dendrite growth[6–13], HER is more difficult to restrain because it is a spontaneous parasitic reaction between ZMA and water molecules in the electrolyte, which constantly consumes the active mass of ZMA and causes a safety concern over the generation of flammable H_2 gas[14]. To suppress the HER, one strategy is to raise the ZMA oxidation potential, for example, by plating on a more stable (0002) lattice plane of zinc[7]. Another is to improve the cathodic stability of water by using water-in-salt electrolytes[12,15,16], deep eutectic solvents[17] and molecular-crowded electrolytes[18,19]. Additionally, various strategies have been reported to stabilize the ZMA surface, including forming a solid electrolyte interphase (SEI)

[1]Department of Chemistry, Oregon State University, Corvallis, OR, USA. [2]GROTTHUSS INC., Corvallis, Oregon, USA. [3]Department of Materials Science and Engineering, University of California, Riverside, CA, USA. [4]Department of Nuclear Science and Engineering, Massachusetts Institute of Technology, Cambridge, MA, USA. [5]Department of Mechanical Engineering, The Pennsylvania State University, University Park, PA, USA. [6]Hewlett-Packard Co., Corvallis, OR, USA. ✉e-mail: agreaney@engr.ucr.edu; chong.fang@oregonstate.edu; david.ji@oregonstate.edu

layer[10,20–24], modifying the solvation structures of Zn ions[16,25,26] and stabilizing the local pH[27].

Nevertheless, most reported CE values were measured at a current density of 1 mA cm^{-2} or above (Supplementary Table 1). It is known that the measured CE is proportional to the applied current density, where the high current densities tend to mask the consequences of HER. Therefore, the reported high CE values cannot ward off battery failures due to cell swelling or electrolyte leaking as hydrogen gas builds up[28]. A stringent test setup to reveal the consequences of the HER is the pouch cell that quickly puffs up if gas is evolved; however, prototype pouch cells free of HER over long-term cycling are rarely reported.

In this Article, we explore the design principles for the electrolyte formula free from dendrite growth and HER (Supplementary Fig. 1). The reduced Hammett acidity of the hybrid electrolyte and the formation of a dual-layered SEI enable an average Zn plating/stripping CE of 99.95% measured at 0.2 mA cm^{-2}. Leveraging on the near-unity CE, the VOPO$_4$·2H$_2$O||Zn Swagelok cells retain 80% of the initial capacity over 4,300 cycles with a negative/positive electrode capacity ratio (N/P ratio) of 2, equivalent to a CE of 99.97%. Moreover, the pouch cell achieves an energy density of 100 Wh kg^{-1} based on the mass of both electrodes and delivers a stable cycling performance over 500 cycles with a limited electrolyte supply of 8.8 ml Ah^{-1}, an N/P ratio of 2.3, and a cathode areal capacity of 2.5 mAh cm^{-2}.

Results
Stripping and plating reversibility of ZMA

Aqueous electrolytes containing Zn^{2+} ions usually exhibit high Brøn-sted–Lowry (BL) acidity because Zn^{2+} weakens the O–H bonds of aqua ligands. One strategy to lower the acidity of such electrolytes is to replace the aqua ligands of Zn^{2+} with stronger Lewis bases. In particular, adding chloride to 30 m ZnCl$_2$ (30Z) can transform hydrated Zn^{2+} to Zn–Cl complex ions such as [ZnCl$_4$]$^{2-}$ (refs. [16,25,29]). Our previous studies showed that mixing LiCl in 30Z can increase the CE of ZMA from 98.0 to 99.7% tested at 1 mA cm^{-2}, where the screening effect of Li$^+$ suppresses dendrite growth during Zn plating[16]. However, HER was not sufficiently suppressed at lower current densities, so when the current density is reduced to 0.2 mA cm^{-2}, the measured CE drops to 97.63%. Here, we better mimic the conditions of commercial ZMBs to measure the average CE of a commercial Zn metal foil using a modified galvanostatic technique (see Methods for detailed information)[30–32].

Starting with the baseline electrolyte of 30 m ZnCl$_2$ + 5 m LiCl (referred to as ZL), we first examined the benefits of adding one more chloride salt, with the goal of making excess Cl$^-$ displace H$_2$O from the Zn^{2+} solvation sheaths. The selection criterion for this additional chloride salt was that its cation should be a weak Lewis acid so as not to increase the BL acidity of the electrolyte. The methylated ammonium chlorides were selected, and in a systematic study of the number of methyl groups, trimethylammonium chloride (TMACl) stood out, delivering the highest CE (Supplementary Fig. 2a). In particular, the CE of ZMA in ZL + 10 m TMACl (ZLT) was the highest among different concentrations of TMACl (Supplementary Fig. 2b). As shown in Fig. 1a, the average CE of ZLT at 0.2 mA cm^{-2} is 99.60%, much higher than the CEs of 30Z (95.38%) and ZL (97.63%).

Organic molecules may also substitute for H$_2$O in the Zn^{2+} solvation sheaths and reduce the electrolyte's Hammett acidity to suppress HER[25,33]. To harness this mechanism, we investigated several organic co-solvents (Supplementary Fig. 2c). Among them, dimethyl carbonate (DMC) demonstrated the highest average CE of 99.95% at a current density of 0.2 mA cm^{-2} (Fig. 1b). This near-unity CE at such a low current density is unprecedented compared with all previous reported CE values of ZMA (Supplementary Table 1). We chose the 5:1 molar ratio of water and DMC (referred to as ZLT-DMC) for its optimal CE (Supplementary Fig. 2d); this water:DMC molar ratio is far more than the flammable threshold, rendering it a safe electrolyte (Supplementary Fig. 3). In ZLT-DMC, ZMA exhibits excellent cycling stability, rate capability, and

HER-free and anticorrosion properties (Supplementary Figs. 4 and 5). In addition to the high CE, ZLT-DMC has a lower density of 1.69 g cm^{-3} than ZL and ZLT, allowing a smaller mass of electrolyte to wet the cell, thereby benefiting the energy density (Fig. 1a). Furthermore, ZLT-DMC has a conductivity of 15 mS cm^{-1}, which is higher than those of ZLT and ZL (Supplementary Fig. 6).

The unique Zn-ion solvation structure

The near-unity CE of ZMA reflects almost complete suppression of the HER (see the gas chromatography results in Supplementary Fig. 7). How does ZLT-DMC enable this? First, does ZLT-DMC have a low acidity? We measured the Hammett acidity of the electrolytes with 4-chloro-2-nitroaniline as an indicator (Supplementary Fig. 8)[34]. Adding TMACl reduces the electrolyte's Hammett acidity by turning it into a weaker proton donor (Fig. 1c). The calculated Hammett acidity changes from −2.07 for 30Z and −2.13 for ZL to −1.33 for ZLT. This result confirms our postulation that the electrolyte is less acidic when the primary cations are switched from hydrated Zn^{2+} to hydrated weak Lewis acid cations, that is, TMA$^+$. Moreover, adding DMC further reduces the acidity, raising the Hammett acidity value to −0.67. In addition, the ^{1}H nuclear magnetic resonance (NMR) spectra of water shift up-field from 4.62 parts per million (ppm) in 30Z to 4.55 ppm in ZLT-DMC, compared with 4.70 ppm in pure water, indicating that the protons of water are more shielded with a higher electron density (Fig. 1d). The calculated T_1 relaxation time of ^{1}H is 0.660 s for ZLT-DMC, much shorter than the ~4 s for pure water, revealing the weakened interactions between water and its environment and corroborating the lowered acidity of the electrolyte (Supplementary Fig. 9).

Second, besides the reduced acidity, how does the local environment of water change upon adding TMACl and DMC to the electrolyte? In the low-frequency region of the femtosecond stimulated Raman spectra (FSRS), the peaks at ~380, 293 and 240 cm^{-1} are attributed to the Zn–O vibration in [Zn(OH$_2$)$_6$]$^{2+}$, the Zn–Cl vibration in [ZnCl$_4$]$^{2-}$ and the vibrations of the polynuclear Zn–Cl aggregates bridged by Cl$^-$, respectively (Fig. 1e). Increasing the TMACl's concentration in ZL decreases the peak at 380 cm^{-1} and strengthens the peak at 293 cm^{-1}, consistent with the notion of dehydration of [Zn(OH$_2$)$_6$]$^{2+}$ due to the formation of more Zn–Cl complex ions (Supplementary Fig. 10a). Moreover, introducing bulky TMA$^+$ cations could depolymerize the Zn–Cl aggregates, as indicated by the diminished peak at 240 cm^{-1}. The blue shift of water's bending mode via addition of TMACl in ZL suggests the dehydration of Zn ions (Supplementary Fig. 10b). The lowered peak intensity represents the decreased polarizability of water. Therefore, the Raman results indicate that adding TMACl reduces the presence of H$_2$O in the solvation sheaths of Zn^{2+}, which helps strengthen the O–H bonds of water.

The O–H stretching for water in the high-frequency range (Fig. 1f) can be deconvoluted into three peaks corresponding to different hydrogen-bonding environments (Supplementary Fig. 11). From pure water to 30Z, most water molecules transition from the double donor-double acceptor conformation to the donor-acceptor (DA) conformation as part of the Zn^{2+} hydration shell[35,36]. Furthermore, the DA mode blue-shifts upon addition of LiCl in 30Z and stiffens again upon addition of TMACl with lowered peak intensity (Supplementary Table 2). This blue shift arises from water molecules being surrounded by electron-donating [ZnCl$_4$]$^{2-}$ anions and TMA$^+$ cations—a weaker Lewis acid than water. The lowered DA peak intensity again reveals the mitigated electric polarizability of water due to an increasing concentration of less-polarizing ions[37].

Third, how does DMC affect the chemical environment of the electrolyte? DMC is immiscible in water or dilute aqueous electrolytes but becomes miscible in concentrated ZnCl$_2$ solutions (Supplementary Fig. 12)[38]. Adding organic co-solvents such as dimethylsulfoxide to aqueous electrolytes was previously attempted to improve the CE of ZMA, where dimethylsulfoxide enters the Zn^{2+} solvation sheaths to
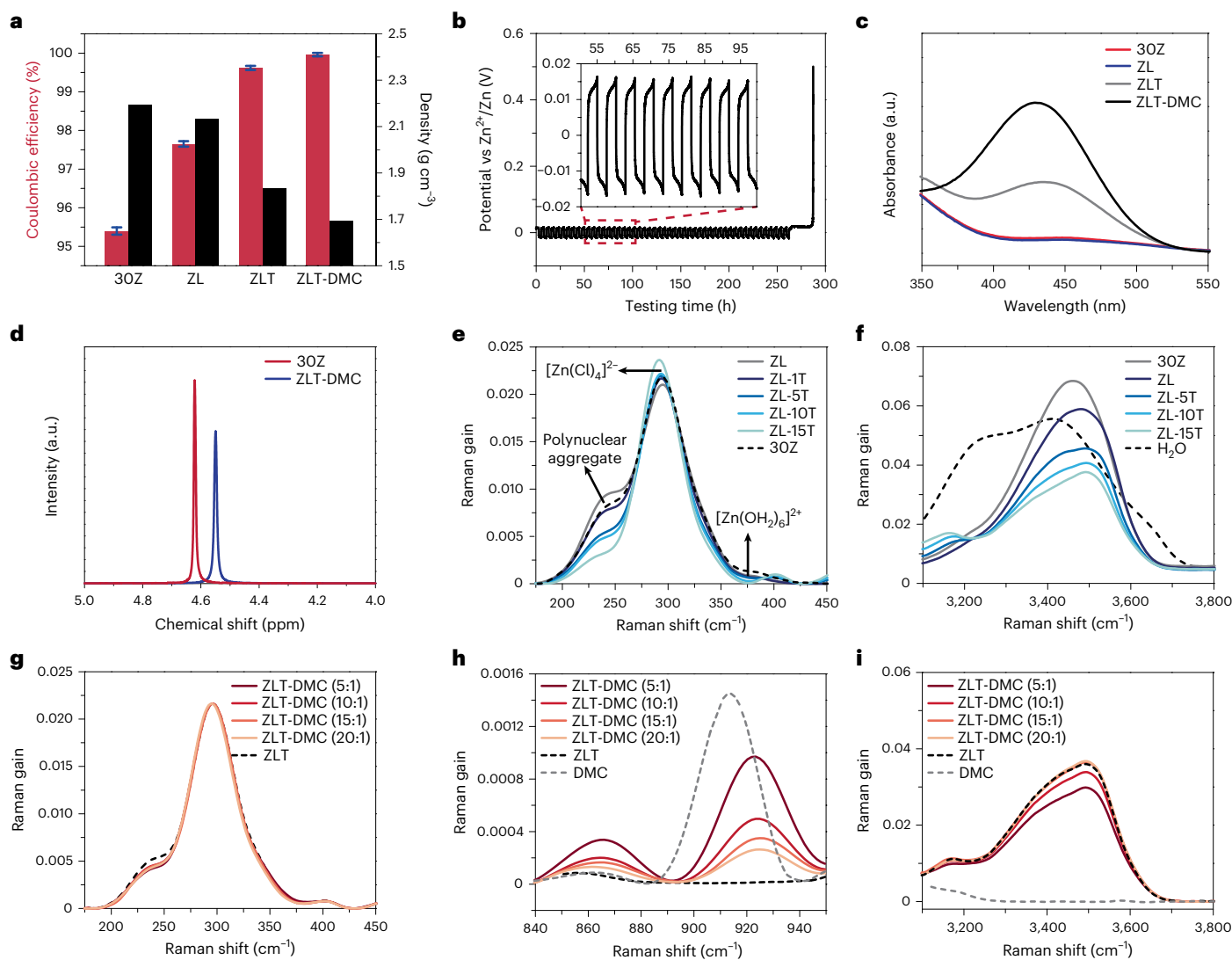
Fig. 1 | Reversibility of ZMA and properties of the electrolytes. a, Average CE values of ZMA in different electrolytes measured at 0.2 mA cm^{-2} (red) with error bars (blue) and the density of electrolytes (black). For CE values, data are presented as mean ± s.d. (n = 3). s.d., standard deviation. **b**, The GCD potential profiles for the average CE measurement in ZLT-DMC at 0.2 mA cm^{-2}. Inset: enlarged GCD potential profiles showing the extent of overpotential.

c, Absorption spectra of 4-chloro-2-nitroaniline indicator in different electrolytes for measuring the Hammett acidity. **d**, Water's ^{1}H NMR spectra of 3OZ (red) and ZLT-DMC (blue). **e,f**, FSRS spectra of ZL with different concentrations of TMACl in the low-frequency region (**e**) and high-frequency region (**f**). **g–i**, FSRS spectra of ZLT with different H$_2$O/DMC molar ratios in the low-frequency region (**g**), middle-frequency region (**h**) and high-frequency region (**i**).

suppress HER[25]. In contrast, the DMC molecules with a lower donor number (16.0) barely solvate Zn^{2+} cations in ZLT-DMC, as revealed by our FSRS and ab initio molecular dynamics (AIMD) calculations (Supplementary Fig. 13). The Zn−Cl vibrational modes remain unchanged upon increasing the DMC:H$_2$O molar ratio from 1:20 to 1:5, indicating that DMC is a weaker Lewis base than either Cl$^-$ or water to solvate Zn^{2+} (Fig. 1g). However, DMC does interact with water. The O−C−O stretching mode of DMC at ~910 cm^{-1} in Raman studies splits into two peaks at ~860 and 925 cm^{-1}, which suggests that the interactions between DMC and H$_2$O break the O−C−O symmetry (Fig. 1h), consistent with a shortened T_1 relaxation time seen in the ^{1}H NMR results. The DMC addition does not blue-shift the bending and stretching modes of water but lowers the Raman peak intensity (Supplementary Fig. 14). Therefore, similar to TMACl, DMC further decreases the electric polarizability of water molecules (Fig. 1i). As a result, ZLT-DMC exhibits an expanded thermodynamic stability window of 2.39 V (Supplementary Fig. 15)[15,39]. A critical question is whether DMC alone is sufficient to transform the properties of 3OZ in achieving the high CE of ZMA. Nevertheless, adding

DMC improves the CE of 3OZ from 95.38% to 98.36% for 3OZ-DMC tested at 0.2 mA cm^{-2}, although this is still lower than that of ZLT-DMC.

The structure and morphology of plated ZMA

Ex situ X-ray diffraction patterns confirm that the ZMA surface is free of insoluble Zn(OH)$_2$-based precipitation phases after 200 cycles in ZLT-DMC (Supplementary Fig. 16)[33,40]. After cycling, the ZMA surface is flat in contrast to the 'mountainous' topography generated in 3OZ (Fig. 2a,b). In ZLT-DMC, the surface of ZMA shows no dendrites, and the plated mass contains no holes or cracks, as evidenced by scanning electron microscopy (SEM) imaging of the cross-section carved by a focused ion beam (FIB) (Fig. 2c and Supplementary Fig. 17). Furthermore, using in situ optical microscopy, resistance to dendrite formation was further investigated by real-time observation of Zn plating at the high current density of 10 mA cm^{-2} (Supplementary Fig. 18 and Supplementary Videos 1–5). In 3OZ, the plated Zn became rough with dendrite formation after 40 min of plating (Fig. 2d). In contrast, the ZLT-DMC electrolyte enabled flat and compact Zn plating over 120 min (Fig. 2e). The plated
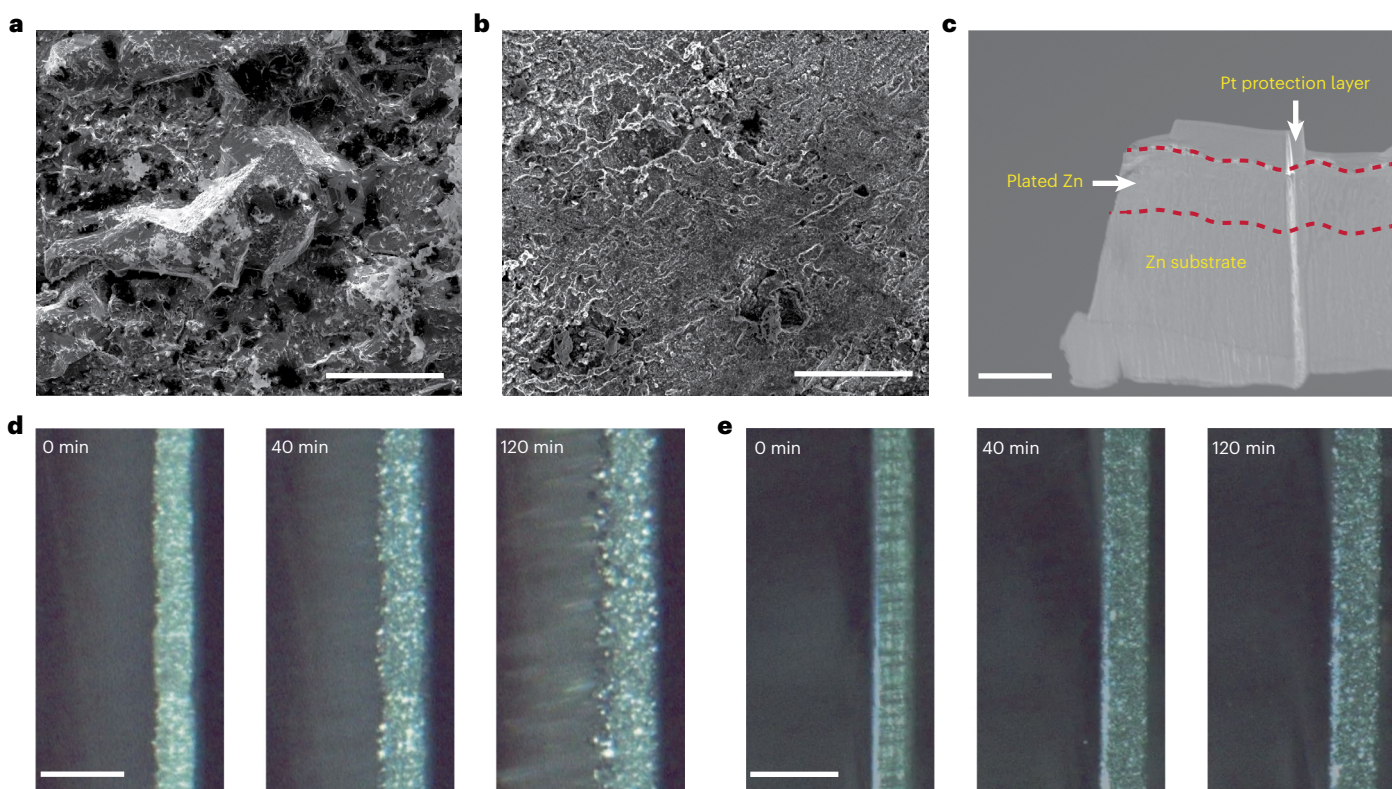
Fig. 2 | Physical characterization of ZMA in 30Z and ZLT-DMC electrolytes. **a,b**, SEM images of ZMA after 200 cycles with an areal capacity of 1 mAh cm^{-2} at a current density of 1 mA cm^{-2} in 30Z (**a**) and ZLT-DMC (**b**). Scale bar, 25 µm. **c**, The cross-sectional SEM image of the ZMA surface region collected after 200 cycles in ZLT-DMC. Pt coating on the Zn surface was used for the FIB lifting-out process. Scale bar, 2 µm. **d,e**, In situ optical microscopy images of ZMA plating (side view) in 30Z (**d**) and ZLT-DMC (**e**) at a current density of 10 mA cm^{-2} and up to 120 min. Scale bar, 200 µm.

Zn in ZLT-DMC is 35.7 µm in thickness, matching the theoretical 34.2 µm corresponding to the plated capacity of 20 mAh cm^{-2}. However, the plated Zn in 30Z is around 55 µm thick, indicating porosity and surface roughness. We also investigated ZMA plating in 30Z-DMC, ZL, and ZLT electrolytes, finding their overall performances to be better than that of 30Z but worse than that of ZLT-DMC (Supplementary Fig. 19).

Dual-layered SEI on ZMA

The extremely high CE and dendrite-free morphology indicate that an SEI layer forms to passivate the ZMA surface[41,42]. We examined the surface structure of the plated ZMA in ZLT-DMC by observing the FIB-prepared cross-section of the surface region with transmission electron microscopy (TEM). The cross-section displays a distinct surface layer on top of the bulk Zn substrate (Fig. 3a). The surface layer has a uniform thickness below 200 nm, comprising inner and outer layers judging from the imaging contrast (Fig. 3b). The energy-dispersive X-ray spectroscopy elemental mappings associated with the dark-field scanning TEM (STEM) delineate the uniform dispersion of Zn, Cl, and O in this layer, where the C signal is characteristic of the outer SEI layer (Supplementary Fig. 20).

More quantitative analysis by X-ray photoelectron spectroscopy (XPS) revealed the depth-profiled composition throughout the SEI. Only the outer SEI layer contains notable C 1s signals, which can be deconvoluted into three components (Fig. 3d). The peaks at ~284.8 and ~286.3 eV are assigned to C–C/C–H and C–O bonds, respectively, while the ~289.0 eV peak is ascribed to the carbonate of –OCO$_2$–. We attribute the existence of these organic moieties to the reduction of DMC (Fig. 3c). After Ar$^+$ sputtering for 1 min, the C 1s peak intensity drops to half that on the top surface, and after sputtering for 9 min, the peak intensity remains just above the noise level, suggesting that the outer SEI layer is ca. 60 nm thick (Fig. 3d and Supplementary Fig. 21).

The O 1s signal matches the trend of the C 1s signal, where the total percentage of O–C and O=C progressively decreases upon Ar$^+$ sputtering, but the O–Zn oxygen signal persists until 200 nm deep, beyond which the SEI layer transitions to metallic Zn (Supplementary Fig. 22a). Furthermore, the Zn 2p$_{3/2}$ signal of Zn–Cl at 1,023 eV also persists throughout the SEI layer, constituting the inner inorganic SEI layer with Zn–O species (Fig. 3e). In the Cl 2p spectrum, both Zn–Cl and oxychloride are distinct in the outer SEI layer (Supplementary Fig. 22b)[22]. Deeper into the inner SEI layer, the percentage of oxychloride decreases, but the Zn–Cl signals still dominate, consistent with the Zn 2p$_{3/2}$ result (Fig. 3e). Pulling together the microscopy and XPS results, we conclude that the ZMA's SEI layer formed in the ZLT-DMC electrolyte comprises an outer organic/inorganic composite layer and an inner inorganic layer (Fig. 3c). We also collected depth-profiled XPS spectra for ZMAs cycled in all the other permutations of electrolytes (Supplementary Figs. 21 and 23). Overall, the SEI layers formed in the pure inorganic electrolytes of 30Z, ZL, and ZLT are much thicker and contain more oxides than those in ZLT-DMC.

The disparity in CE values and composition profiles between ZLT-DMC and the other baseline electrolytes suggests that the organic moieties are instrumental in passivating the ZMA surface. This begs the question: do these moieties have to come from DMC, or could other ester carbonates perform an identical role? We tested ZMA's CE with diethyl carbonate (DEC) and ethyl methyl carbonate (EMC) added to ZLT with the same 5:1 molar ratio of water and carbonate. At a current density of 0.2 mA cm^{-2}, the CE values are 99.86% and 99.82% for ZLT-DEC and ZLT-EMC, respectively, which are lower than that of ZLT-DMC (Supplementary Fig. 2c). In ZLT-DEC, the cross-sectional STEM image displays a much thicker SEI layer ranging from 500 nm to 1.5 µm (Supplementary Fig. 24). The XPS depth-profiling analysis of this SEI displays a quickly diminished intensity of the C 1s peaks along
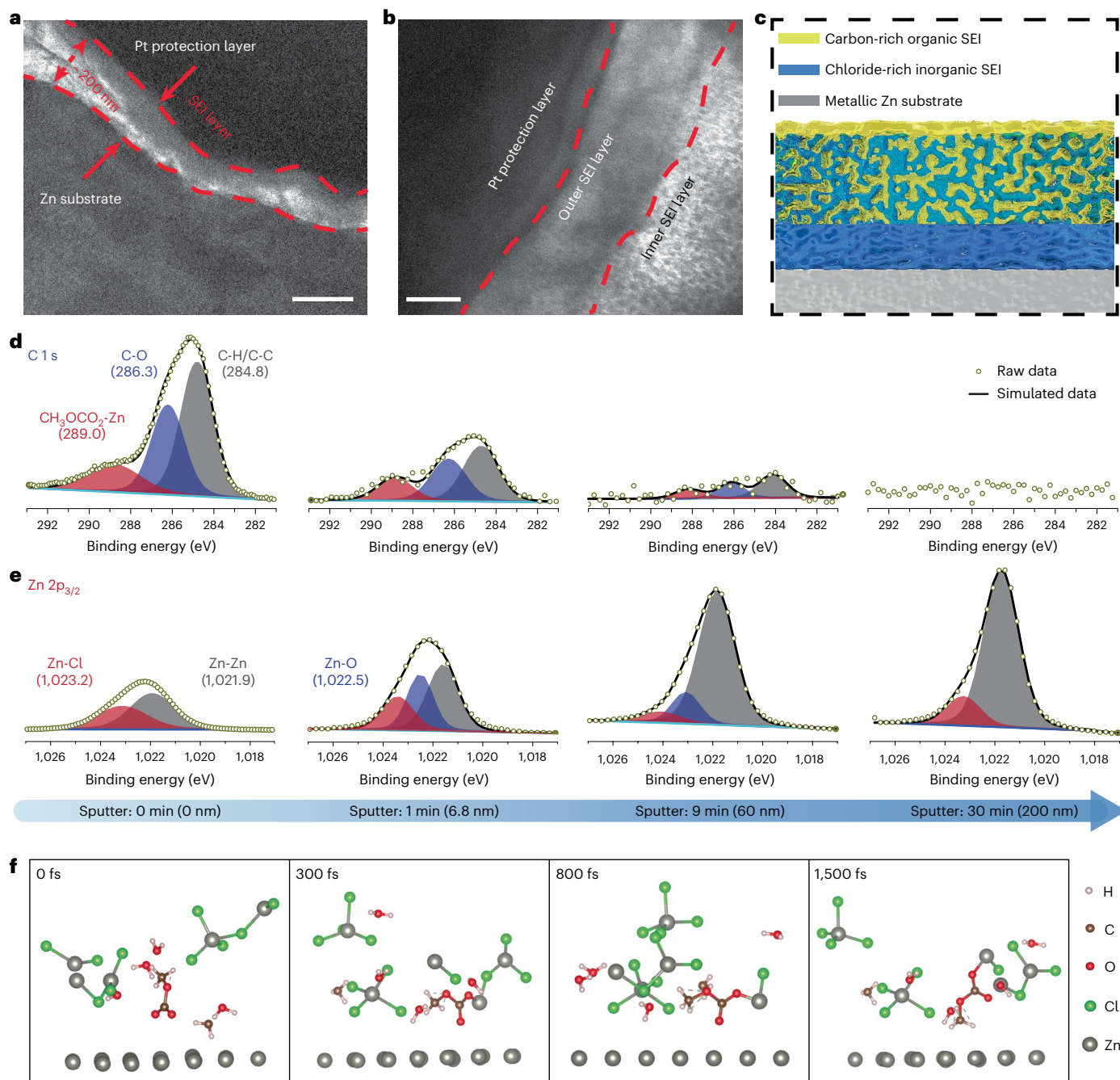
Fig. 3 | Physical characterization of the interfacial chemistry of ZMA in ZLT-DMC. a,b, The cross-sectional TEM image (**a**) and high-resolution TEM image (**b**) of the dual-layered SEI on the ZMA surface. Scale bars, 200 nm (**a**) and 20 nm (**b**). **c,** Schematic presentation of the dual-layer SEI. **d,e,** XPS spectra with depth profiles of C 1s (**d**) and Zn 2p$_{3/2}$ (**e**). **f,** AIMD simulation of the formation process of organic SEI species on the Zn metal surface. The uninvolved molecules are removed from the snapshots (Supplementary Fig. 27).

with Ar$^+$ sputtering, which drops to the noise level after 5 min of sputtering (Supplementary Fig. 25). This indicates that the outer organic SEI layer of ZLT-DEC is thinner than that of ZLT-DMC despite the entire SEI layer being much thicker. The much greater thickness of the SEI here suggests that the formative SEI in ZLT-DEC cannot effectively passivate the ZMA surface and the parasitic SEI formation reaction prolongs the consumption of the ZMA active mass, which explains the lower CE values in ZLT-DEC than in ZLT-DMC. Furthermore, compared with DMC, the less O–C–O stretching mode split of DEC at ~899 cm^{-1} in Raman studies indicates a weaker interaction between DEC and H$_2$O molecules in ZLT-DEC electrolyte with a lower Hammett acidity than ZLT-DMC, resulting in less generation of organic radicals for outer

organic SEI layer formation (Supplementary Fig. 26). It is postulated that the insufficient S$_N$2 ester cleavage and the steric effect of the bulkier sidechains of DEC and EMC inhibit the formation of a dense organic layer on the Zn metal surface. Similarly, adding cyclic carbonates, for example, ethylene carbonate and propylene carbon, delivers even lower CE values than ZLT (Supplementary Fig. 2c).

To further visualize organic SEI formation, we performed AIMD simulations of the ZLT-DMC electrolyte at a ZMA surface under reducing conditions in which the system was prepared with a CH$_3$OOCO radical adjacent to the ZMA surface (Fig. 3f and Supplementary Fig. 27). The CH$_3$OOCO interacts with a Zn–Cl complex ion and forms a Zn$_2$Cl$_3$–O–COOCH$_3$ intermediate compound after 300 femtoseconds (fs),
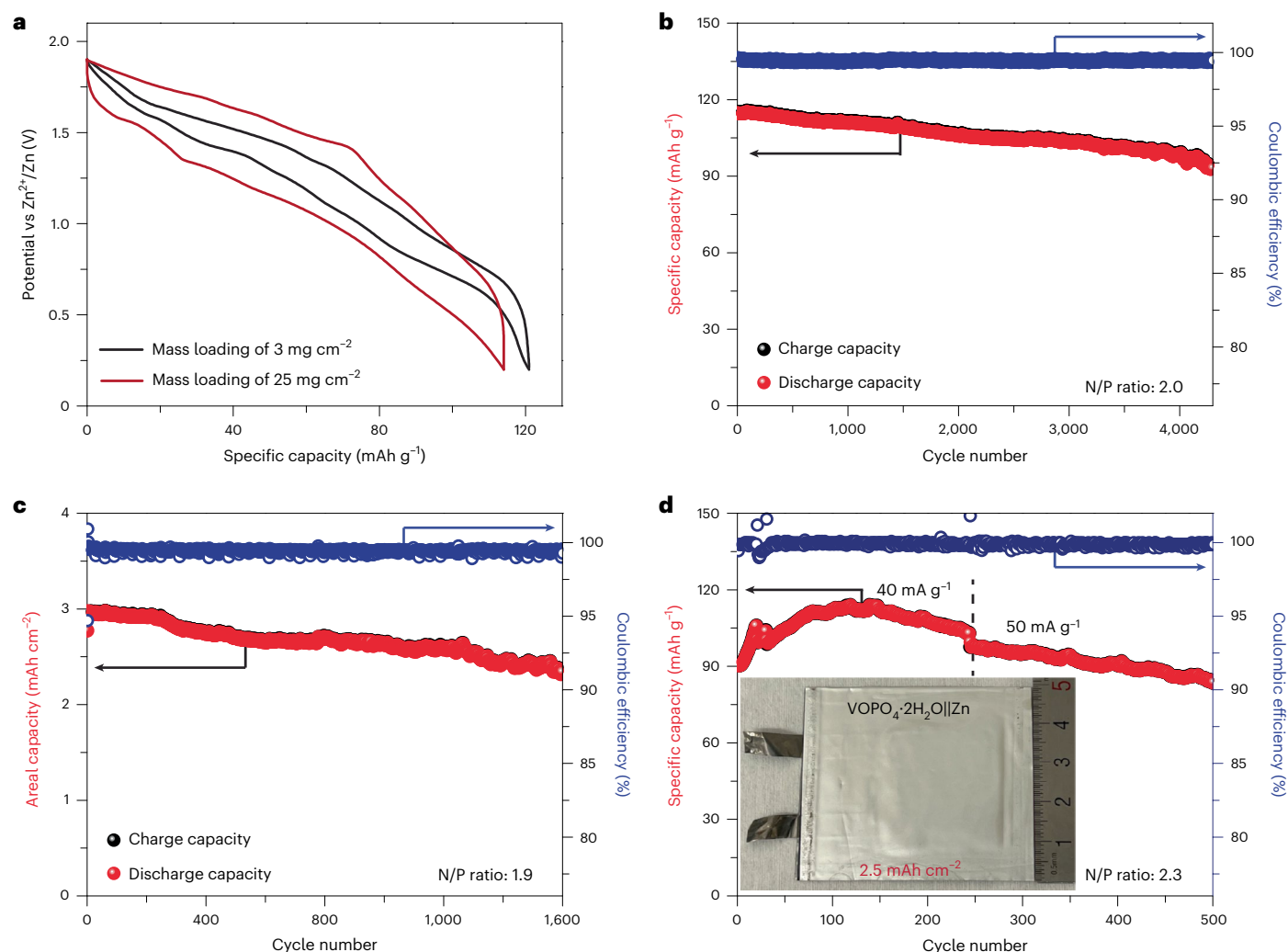
Fig. 4 | Electrochemical performance of VOPO$_4$·2H$_2$O||Zn full cells. a, GCD potential profiles at 0.2 A g^{-1} with different cathode mass loadings tested in a Swagelok cell configuration. **b**, Swagelok cell cycling with a VOPO$_4$·2H$_2$O mass loading of 3 mg cm^{-2} at 2 A g^{-1}. **c**, Swagelok cell cycling with the VOPO$_4$·2H$_2$O mass loading of 25 mg cm^{-2} at 0.3 A g^{-1}. **d**, Pouch cell cycling with VOPO$_4$·2H$_2$O mass loading of 22.5 mg cm^{-2}. Black and red dots represent charge and discharge capacity values (left y axis), respectively, and the blue dots represent CE values (right y axis). The pouch cell was activated at 20 and 30 mA g^{-1} for 20 and 10 cycles, respectively, in the first 30 cycles of cycling. The dashed black line marks the 245th cycle, where the current rate was changed from 40 mA g^{-1} to 50 mA g^{-1}. Inset: digital image of the pouch cell after 500 cycles. See the side image of the same cycled pouch cell in Supplementary Fig. 29f.

which by 800 fs has transformed to ZnCl–O–COOCH$_3$. The simulation was continued for another 700 fs, during which the ZnCl–O–COOCH$_3$ compound remained stable. Another insight from the AIMD simulation of the electrolytes is the importance of LiCl and TMACl for the formation of [ZnCl]$^+$ ions, with the ZLT-DMC electrolyte containing seven times as many [ZnCl]$^+$ ions as 30Z-DMC. This suggests that a sufficient concentration of [ZnCl]$^+$ cations is critical for forming a high-quality organic SEI layer in ZLT-DMC, and this organic layer is essential in passivating the ZMA and suppressing HER[21].

Electrochemical performance of full cells

We further tested the reversibility of ZMA in VOPO$_4$·2H$_2$O||Zn full cell with the ZLT-DMC electrolyte[20,43,44]. The layered VOPO$_4$·2H$_2$O cathode can serve as a stable counter electrode to couple ZMA by exhibiting excellent cycling stability, near-unity CE, and fast rate capability (Supplementary Fig. 28). With a cathode mass loading of 3 mg cm^{-2} and an N/P capacity ratio of 2, the VOPO$_4$·2H$_2$O||Zn full cells in Swagelok cells deliver an energy density of 94 Wh kg^{-1} based on the mass of both electrodes, an average voltage of ~1.1 V and a high round-trip efficiency of ~90% at 0.2 A g^{-1} (Fig. 4a). At a higher current rate of 2 A g^{-1}, this full cell retains

80% of its initial discharge capacity after ~4,300 cycles (Fig. 4b). Next, we increased the cathode active mass loading to ~25 mg cm^{-2}, near that used by commercial batteries. A VOPO$_4$·2H$_2$O free-standing film was paired with 10 μm thick commercial zinc foil to achieve an N/P ratio of 1.9. The cell round-trip efficiency decreases to 75%, but the specific capacity is not compromised. The cathode delivers an areal capacity of ~2.9 mAh cm^{-2}, and the full-cell capacity retention is ~80% after 1,600 cycles at a current rate of 0.3 A g^{-1} (Fig. 4c). Importantly, suppressing the parasitic reactions also enhances the self-discharge performance of full cells. The cell capacity retention is ~91.0% after resting at open circuit voltage for 240 h in ZLT-DMC at room temperature, compared with 91.2% after 24 h in 30Z (Supplementary Fig. 29a,b). The full cell also exhibits a stable low-temperature (−20 °C) cycling performance with a specific capacity of ~89 mAh g^{-1} at the current rate of 0.1 A g^{-1} (Supplementary Fig. 29c–e)[19,33,45,46]. Note that ZLT-DMC exhibits a melting point of −68 °C.

To reveal whether piecemeal HER takes place in ZLT-DMC, we tested single-layer pouch cells with an N/P ratio of 2.3 to check whether non-rigid pouch cells swell due to gas formation. We controlled the electrolyte usage to the level of 8.8 ml Ah^{-1}. The pouch cells operated with an areal capacity of over 2.5 mAh cm^{-2}, storing an energy density of

100 Wh kg^{-1} based on the mass of both electrodes. The pouch cell delivered excellent cycling performance for 500 cycles over 115 d, with no leaking and cell swelling observed (Fig. 4d and Supplementary Fig. 29f).

Discussion

We have developed a hybrid concentrated electrolyte formula that delivers a near-unity CE (99.95%) at a low current density of 0.2 mA cm^{-2}. The Hammett acidity of our electrolyte is reduced due to the combination of several changes: (1) excess chloro ligands replacing H_2O molecules in the Zn^{2+} solvation sheaths by forming Zn–Cl complex ions, (2) the presence of a Lewis acid cation of TMA$^+$ weaker than Zn^{2+} and water, and (3) the interactions between DMC and H_2O. Furthermore, the DMC co-solvent facilitates the in situ formation of an SEI layer comprising an organic/inorganic composite outer layer and an inorganic inner layer. This SEI layer effectively passivates the ZMA to suppress HER and dendrite formation, preventing cell failure and enabling high safety with the non-flammable electrolyte. Building upon the near-unity CE, the VOPO$_4$·2H$_2$O||Zn full cells deliver an excellent cycling performance under practical conditions and the enhanced performance indicates a competitively low levelized energy cost of ZMBs. It is worth noting that concentrated ZnCl$_2$ electrolytes are corrosive to Cu or Al current collectors, and they do not wet the polypropylene separators used in Li-ion batteries. Extensive engineering work is necessary for a new Zn battery technology using this new electrolyte. However, the development of electrolytes free from HER and dendrite growth will go a long way in the commercialization of low-cost and high-safety Zn metal batteries that contribute to the sustainability of global energy supply.

Methods

Materials preparation

The VOPO$_4$·2H$_2$O powder was synthesized according to the literature[47]. The vanadium (V) oxide (>97.0%) and phosphoric acid (ACS reagent, ≥85 wt% (percentage by weight) in H_2O) were purchased from Sigma Aldrich. Typically, 4.8 g of V_2O_5 was mixed with 26.6 ml of 85 wt% H_3PO_4 and 115.4 ml of deionized water. The suspension was sonicated for 30 min before refluxing at 110 °C for 16 h. The as-prepared yellow-green colour VOPO$_4$·2H$_2$O powder was centrifuged, washed with deionized water and kept under ambient conditions (Supplementary Fig. 30). For electrolyte preparation, the TMACl (>97.0%) and anhydrous lithium chloride (>98.0%) were purchased from Tokyo Chemical Industry, and the zinc chloride (metals basis, 99.95%), anhydrous ethanol (HPLC grade), acetone (>99.0%), and water (HPLC grade) were ordered from Alfa Aesar. The DMC, diethyl carbonate, ethyl methyl carbonate, propylene carbonate, ethylene carbonate, and acetonitrile were purchased from BASF (battery grade).

Materials characterization

The surface morphology of cycled Zn metal anodes was viewed using FEI NOVA 230 field-emission scanning electron microscopy. The FIB-SEM was employed to obtain the cross-section samples on a Helios 650 Ultra Resolution Dual Beam FEG SEM, and the SEI layer was investigated using the FEI Titan 80–300 high-resolution TEM with four embedded Bruker SDD detectors. The in situ optical microscopy measurements were conducted with an optical micro zoom inspection system (Scienscope, MZ7A). The beaker cell was connected to the Gamry electrochemical workstation for the galvanostatic plating process (current density of 10 mA cm^{-2} at 25 °C), where Zn foils (100 µm) were used as both working and counter electrodes. The chemical bonding environments were probed by XPS via a PHI VersaProbe III Scanning XPS Microprobe. The system's energy scale was calibrated to Cu 2p$_{3/2}$ at 932.6 eV and Au 4f at 84.0 eV, where the base pressure of the system was $3 × 10^{-7}$ Pa. XPS was performed using monochromatized Al Kα radiation (hv = 1,486.6 eV, at 50 W and 200 µm beam diameter). The electron analyser pass energy was set to 69 eV with an emission angle of 45°. The specimens were neutralized using a combination of an electron flood gun set to 0.6 eV at 20 µA and an ion flood gun set to 0.1 kV. The XPS data were charge corrected to the C 1 s aliphatic carbon binding energy at 284.8 eV. The XPS profiling was performed using a monoatomic argon ion beam at a 2 kV accelerating voltage and 1 µA of current, with a raster area over 2 mm × 2 mm. The sputterring profile data were acquired with a pass energy of 140 eV with an emission angle of 45°. The depth-profiling Ar$^+$ sputtering rate was estimated to be ~6.8 nm min^{-1}, and the SEI compositions were analysed by fitting the whole XPS spectra using CasaXPS software. X-ray diffraction was conducted on a Rigaku Ultima IV diffractometer with Cu Kα radiation ($\lambda = 1.5406$ Å). ^{1}H NMR spectra were collected on a Bruker Ascend 500 NMR spectrometer at a ^{1}H frequency of 500 MHz, with t-butanol as the internal reference. For Hammett acidity measurements, a ultraviolet–visible spectroscopy spectrum Lambda 1050 with an integrated sphere was used to detect the concentration of the indicator in different electrolytes. We evaluated the extent of HER for different electrolytes by running Zn||Zn symmetric beaker cells with a PerkinElmer Clarus 480 gas chromatograph (GC). The GC was equipped with a 5 Å molecular sieve column with Ar as the carrier gas and with a thermal conductivity detector. The beaker cells were first purged with Ar gas before a constant current density of 1 mA cm^{-2} was applied for 3 h, where one Zn electrode was plated and the other Zn electrode was stripped. The GC measurements were conducted using ultra-pure Ar as a carrier gas. The gaseous sample of 200 µl was taken from the headspace of the beaker cell and injected into the GC[48]. Differential scanning calorimetry (DSC) was conducted using Netzsch DSC 200 F3 in the procedure of cooling to −150 °C with a cooling rate of 10 °C min^{-1}, holding at −150 °C for 5 min and heating to 25 °C with a heating rate of 5 °C min^{-1}.

Ground-state (GS)-FSRS measurements

The GS-FSRS setup was built upon a mode-locked Ti:sapphire oscillator (Mantis-5, Coherent) seeded regenerative amplifier (Legend Elite USP-1K-HE, Coherent) with a fundamental laser pulse train output of ~800 nm centre wavelength, 35 fs duration, 3.6 W average power at 1 kHz repetition rate. The picosecond (ps) Raman pump was generated through a home-built three-stage noncollinear optical parametric amplifier system[49]. The fs Raman probe was produced by focusing a small portion of the 800 nm fundamental pulse on a 2-mm-thick quartz cuvette (Spectrosil 1-Q-2, Starna Cells) filled with deionized water and was temporally compressed through a chirped mirror pair (DMC-9, 450–950 nm, Laser Quantum)[50]. The Raman pump and probe pulses were then focused by a reflective parabolic mirror onto a 1-mm-thick quartz cuvette containing various electrolyte samples. Past the sample, only the probe was collimated, refocused and dispersed by a reflective grating inside a spectrograph (IsoPlane SCT-320, Princeton Instruments), and finally imaged on a CCD array camera (PIXIS:100F, Princeton Instruments). During data collection, the Raman pump was tuned to 510 nm with a power of ~3 mW before the phase-stable optical chopper. For the low-frequency (below 2,000 cm^{-1}) and high-frequency (above 3,000 cm^{-1}) spectral data collection, respective gratings with 1,200 and 600 grooves per mm, and blaze wavelengths of 300 nm and 500 nm were used. For subsequent data analysis, the pure water spectrum was subtracted from the low-frequency data before a smooth baseline was drawn and removed to dissect the water H–O–H bending region. In contrast, only the spectral baseline correction was performed for the high-frequency data analysis of the water O–H stretching region.

Theoretical calculations

AIMD simulations were performed to investigate the solvation structure of ZnCl$_2$-based electrolytes, together with the SEI formation process in the ZLT-DMC electrolyte. The Vienna ab initio simulation Package (VASP) with projector augmented wave pseudopotentials and the generalized gradient approximation of Perdew-Burke-Ernzerh were used for the exchange-correlation function. The energy cut-off was 600 eV using a 1 × 1 × 1 Monkhorst-Pack reciprocal space grid of

k-points for a single-unit cell. All systems were monitored for 8 ps with a step size of 0.5 fs, and H was modelled as deuterium. AIMD simulations of SEI were run at 300 K with a 0.5 fs time step for approximately 2 ps by relaxing the ZLT-DMC electrolyte on the surface of the Zn slab. Before adding the Zn slab into the system, the ZLT-DMC electrolyte system was generated with homogeneous mixing of all components at a designed molecular ratio and relaxed for 8 ps to reach the equilibrium of the system. The molecular ratio of $ZnCl_2$:$LiCl$:$TMACl$:H_2O:DMC was 6:2:1:10:2. The volume of the computed cell was calculated on the basis of the experimental electrolyte density.

Electrochemical measurements

For pouch cells, the $VOPO_4 \cdot 2H_2O$ cathode comprises 87.5 wt% active mass, 2.5 wt% single-walled carbon nanotube, and 10 wt% polyvinylidene fluoride binder, which is coated on Ti foils with an active mass loading of ~22.5 mg cm^{-2}. For Swagelok cells, the low-areal-capacity electrodes were composed of 80 wt% active mass, 10 wt% Ketjenblack, and 10 wt% polyvinylidene fluoride coated on carbon fibre paper current collectors with an active mass loading of ~3 mg cm^{-2}; meanwhile, the high-areal capacity electrodes were self-standing films comprising 60 wt% active mass, 30 wt% Ketjenblack, and 10 wt% polytetrafluoroethylene binder with an active mass loading of ~25 mg cm^{-2}. Zn metal foils with different thicknesses were directly used as anode (100 μm and 10 μm foils were purchased from Thermo Fisher and Alibaba, respectively). For the cathode with a low mass loading (~3 mg cm^{-2}), Zn metal pre-deposited on the Ti foil served as the anode with an estimated area capacity of ~0.69 mAh cm^{-2} and a thickness of ~1.2 μm. The pouch cells were assembled and sealed using an MSK-11A-S vacuum sealer with a cathode, anode, and electrolyte mass ratio of 1:0.23:1.5. The amount of ZLT-DMC electrolyte used for the pouch cells was 8.8 ml Ah^{-1} (15 g Ah^{-1}). The galvanostatic charge-discharge (GCD) tests were conducted at room temperature on a Landt CT3002AU system and analysed by LAND software. The accuracy of the Landt CT3002AU is 0.05% at the current range of 1 mA, corresponding to 0.5 μA. The constant current applied for the CE tests was 0.217 mA based on the current density of 0.2 mA cm^{-2}; thus, the accuracy for each cycle equalled $\frac{0.5 \text{ A}}{0.217 \text{ mA}} = 0.23\%$. When we tested 50 cycles to measure the average CE, the instrument error was much smaller than 0.23%, whereas if a power law of the square root was applied, the error for the CE values was $\frac{0.23\%}{\sqrt{50}} = 0.033\%$. The capacity values of the cathode were calculated on the basis of the active mass of the $VOPO_4 \cdot 2H_2O$ cathode; however, the energy density of the full cells was derived from the total mass of both electrodes. Cyclic voltammetry and electrochemical impedance spectroscopy were performed on a VMP-3 multichannel workstation, and data were analysed using EC-lab and Zview, respectively. The cycled ZMA samples were achieved by employing Zn metal as both the working electrode and counter electrode in a beaker-type symmetric cell. Before ex situ measurements, the electrodes were carefully rinsed in deionized water and dried under vacuum.

We conducted a modified galvanostatic technique to evaluate the key factors affecting Zn reversibility and reveal the accurate Zn plating/stripping CE. We used a Zn foil as the reservoir with a specific areal capacity ((Q_t = theoretical capacity × utilization%). The utilization % of the Zn metal anode (96.14%) was measured by a complete stripping process compared to the theoretical capacity based on the Zn mass. The number used in this paper was calculated from the average value of ten trials (Supplementary Fig. 5a). In the tests, a fixed fraction of Q_s was directly stripped from the Zn reservoir, followed by plating of the equal capacity (Q_c). After running several cycles (n), the final stripping process was conducted to a preselected upper cut-off potential, which corresponds to the remaining Zn (Q_s). The average CE can be calculated according to equation (1):

$$CE = \frac{n \times Q_c + Q_s}{n \times Q_c + Q_t} \qquad (1)$$

Reporting summary

Further information on research design is available in the Nature Portfolio Reporting Summary linked to this article.

Data availability

The data that support the findings of this study are available in the Article and its Supplementary Information.

References

1. Bauer, C. et al. Charging sustainable batteries. *Nat. Sustain.* **5**, 176–178 (2022).
2. Grey, C. & Tarascon, J. Sustainability and in situ monitoring in battery development. *Nat. Mater.* **16**, 45–56 (2017).
3. Li, C., Jin, S., Archer, L. A. & Nazar, L. F. Toward practical aqueous zinc-ion batteries for electrochemical energy storage. *Joule* **6**, 1727–1742 (2022).
4. Liu, C., Xie, X., Lu, B., Zhou, J. & Liang, S. Electrolyte strategies toward better zinc-ion batteries. *ACS Energy Lett.* **6**, 1015–1033 (2021).
5. Song, J., Xu, K., Liu, N., Reed, D. & Li, X. Crossroads in the renaissance of rechargeable aqueous zinc batteries. *Mater. Today* **45**, 191–212 (2021).
6. Wang, S.-B. et al. Lamella-nanostructured eutectic zinc–aluminum alloys as reversible and dendrite-free anodes for aqueous rechargeable batteries. *Nat. Commun.* **11**, 1634 (2020).
7. Zheng, J. et al. Reversible epitaxial electrodeposition of metals in battery anodes. *Science* **366**, 645–648 (2019).
8. Ma, L. et al. Hydrogen-free and dendrite-free all-solid-state Zn-ion batteries. *Adv. Mater.* **32**, 1908121 (2020).
9. Zeng, Y. et al. Dendrite-free zinc deposition induced by multifunctional CNT frameworks for stable flexible Zn-ion batteries. *Adv. Mater.* **31**, 1903675 (2019).
10. Qiu, H. et al. Zinc anode-compatible in-situ solid electrolyte interphase via cation solvation modulation. *Nat. Commun.* **10**, 5374 (2019).
11. Wang, Z. et al. A metal-organic framework host for highly reversible dendrite-free zinc metal anodes. *Joule* **3**, 1289–1300 (2019).
12. Wang, F. et al. Highly reversible zinc metal anode for aqueous batteries. *Nat. Mater.* **17**, 543–549 (2018).
13. Zheng, J. & Archer, L. A. Controlling electrochemical growth of metallic zinc electrodes: toward affordable rechargeable energy storage systems. *Sci. Adv.* **7**, eabe0219 (2021).
14. Xie, X. et al. Manipulating the ion-transfer kinetics and interface stability for high-performance zinc metal anodes. *Energy Environ. Sci.* **13**, 503–510 (2020).
15. Suo, L. et al. "Water-in-salt" electrolyte enables high-voltage aqueous lithium-ion chemistries. *Science* **350**, 938–943 (2015).
16. Zhang, C. et al. The electrolyte comprising more robust water and superhalides transforms Zn-metal anode reversibly and dendrite-free. *Carbon Energy* **3**, 339–348 (2021).
17. Zhao, J. et al. "Water-in-deep eutectic solvent" electrolytes enable zinc metal anodes for rechargeable aqueous batteries. *Nano Energy* **57**, 625–634 (2019).
18. Xie, J., Liang, Z. & Lu, Y.-C. Molecular crowding electrolytes for high-voltage aqueous batteries. *Nat. Mater.* **19**, 1006–1011 (2020).
19. Han, D. et al. A non-flammable hydrous organic electrolyte for sustainable zinc batteries. *Nat. Sustain.* **5**, 205–213 (2022).
20. Cao, L. et al. Fluorinated interphase enables reversible aqueous zinc battery chemistries. *Nat. Nanotechnol.* **16**, 902–910 (2021).
21. Yuan, L. et al. Regulation methods for the Zn/electrolyte interphase and the effectiveness evaluation in aqueous Zn-ion batteries. *Energy Environ. Sci.* **14**, 5669–5689 (2021).
22. Li, C. et al. Highly reversible Zn anode with a practical areal capacity enabled by a sustainable electrolyte and superacid interfacial chemistry. *Joule* **6**, 1103–1120 (2022).

23. Zhao, Z. et al. Horizontally arranged zinc platelet electrodeposits modulated by fluorinated covalent organic framework film for high-rate and durable aqueous zinc ion batteries. *Nat. Commun.* **12**, 6606 (2021).

24. Li, D., Cao, L., Deng, T., Liu, S. & Wang, C. Design of a solid electrolyte interphase for aqueous Zn batteries. *Angew. Chem. Int. Ed.* **60**, 13035–13041 (2021).

25. Cao, L. et al. Solvation structure design for aqueous Zn metal batteries. *J. Am. Chem. Soc.* **142**, 21404–21409 (2020).

26. Zhang, Q. et al. Designing anion-type water-free Zn^{2+} solvation structure for robust Zn metal anode. *Angew. Chem. Int. Ed.* **133**, 23545–23552 (2021).

27. Yang, H. et al. Constructing a super-saturated electrolyte front surface for stable rechargeable aqueous zinc batteries. *Angew. Chem. Int. Ed.* **59**, 9377–9381 (2020).

28. Sui, Y. & Ji, X. Anticatalytic strategies to suppress water electrolysis in aqueous batteries. *Chem. Rev.* **121**, 6654–6695 (2021).

29. Pang, Q. et al. Fast-charging aluminium–chalcogen batteries resistant to dendritic shorting. *Nature* **608**, 704–711 (2022).

30. Ma, L. et al. Realizing high zinc reversibility in rechargeable batteries. *Nat. Energy* **5**, 743–749 (2020).

31. Adams, B. D., Zheng, J., Ren, X., Xu, W. & Zhang, J. G. Accurate determination of coulombic efficiency for lithium metal anodes and lithium metal batteries. *Adv. Energy Mater.* **8**, 1702097 (2018).

32. Ma, L. et al. Critical factors dictating reversibility of the zinc metal anode. *Energy Environ. Mater.* **3**, 516–521 (2020).

33. Hao, J. et al. Boosting zinc electrode reversibility in aqueous electrolytes by using low-cost antisolvents. *Angew. Chem. Int. Ed.* **60**, 7366–7375 (2021).

34. Duffy, J. & Ingram, M. Acidic nature of metal aquo complexes: proton-transfer equilibriums in concentrated aqueous media. *Inorg. Chem.* **17**, 2798–2802 (1978).

35. Sun, Q. Local statistical interpretation for water structure. *Chem. Phys. Lett.* **568**, 90–94 (2013).

36. Choe, C., Lademann, J. & Darvin, M. E. Depth profiles of hydrogen bound water molecule types and their relation to lipid and protein interaction in the human stratum corneum in vivo. *Analyst* **141**, 6329–6337 (2016).

37. Hwang, H. et al. Hydration breaking and chemical ordering in a levitated NaCl solution droplet beyond the metastable zone width limit: evidence for the early stage of two-step nucleation. *Chem. Sci.* **12**, 179–187 (2021).

38. Wang, F. et al. Hybrid aqueous/non-aqueous electrolyte for safe and high-energy Li-ion batteries. *Joule* **2**, 927–937 (2018).

39. Yang, C. et al. Aqueous Li-ion battery enabled by halogen conversion–intercalation chemistry in graphite. *Nature* **569**, 245–250 (2019).

40. Sun, W. et al. A rechargeable zinc-air battery based on zinc peroxide chemistry. *Science* **371**, 46–51 (2021).

41. Peled, E. The electrochemical behavior of alkali and alkaline earth metals in nonaqueous battery systems—the solid electrolyte interphase model. *J. Electrochem. Soc.* **126**, 2047 (1979).

42. Peled, E. & Menkin, S. SEI: past, present and future. *J. Electrochem. Soc.* **164**, A1703 (2017).

43. Cao, L. et al. Highly reversible aqueous zinc batteries enabled by Zincophilic–Zincophobic interfacial layers and interrupted hydrogen-bond electrolytes. *Angew. Chem. Int. Ed.* **60**, 18845–18851 (2021).

44. Yuan, Y. et al. Understanding intercalation chemistry for sustainable aqueous zinc–manganese dioxide batteries. *Nat. Sustain.* **5**, 890–898 (2022).

45. Zhang, Q. et al. Modulating electrolyte structure for ultralow temperature aqueous zinc batteries. *Nat. Commun.* **11**, 4463 (2020).

46. Ge, J., Fan, L., Rao, A. M., Zhou, J. & Lu, B. Surface-substituted Prussian blue analogue cathode for sustainable potassium-ion batteries. *Nat. Sustain.* **5**, 225–234 (2022).

47. Wang, F. et al. How water accelerates bivalent ion diffusion at the electrolyte/electrode interface. *Angew. Chem. Int. Ed.* **57**, 11978–11981 (2018).

48. Chiu, N. et al. Designing dual-functional metal–organic frameworks for photocatalysis. *Chem. Mater.* **34**, 8798–8807 (2022).

49. Zhu, L., Liu, W. & Fang, C. A versatile femtosecond stimulated Raman spectroscopy setup with tunable pulses in the visible to near infrared. *Appl. Phys. Lett.* **105**, 041106 (2014).

50. Tang, L. et al. Excited state structural evolution of a GFP single-site mutant tracked by tunable femtosecond-stimulated Raman spectroscopy. *Molecules* **23**, 2226 (2018).

Acknowledgements

Author contributions

X.J. conceived the concept for the research. H.J. designed the experiments and analysed data with assistance from S.K.S., G.L., D.H. and J.J.H. GS-FSRS measurements were performed by L.T. under the guidance of C.F. P.A.G. supervised the AIMD simulation that Y.F. carried out. J.L. supervised the in situ optical microscopies that S.W. performed. D.H. and N.-C.C. performed the ultraviolet–visible spectroscopy and gas chromatography tests under the supervision of K.C.S. A.M.S. collected the nuclear magnetic resonance data, and W.F.S. conducted the X-ray photoelectron spectroscopy measurements. X.J., C.F., P.A.G., J.L. and D.W. supervised the project. All authors contributed to interpreting the results, discussed the data and reviewed the final draft.

Competing interests

X.J. and H.J. are inventors on US patent application no. 17/867,672 filed by GROTTHUSS INC. regarding the formula of the electrolytes described in this Article. The other authors declare no competing interests.

Additional information

Supplementary information The online version contains supplementary material available at https://doi.org/10.1038/s41893-023-01092-x.

Correspondence and requests for materials should be addressed to P. Alex Greaney, Chong Fang or Xiulei Ji.

Peer review information *Nature Sustainability* thanks Longsheng Cao and the other, anonymous, reviewer(s) for their contribution to the peer review of this work.

Reprints and permissions information is available at www.nature.com/reprints.

nature portfolio

Corresponding author(s): Alex Greaney, Chong Fang, Xiulei Ji

Last updated by author(s): Feb-3, 2023

Reporting Summary

Nature Portfolio wishes to improve the reproducibility of the work that we publish. This form provides structure for consistency and transparency in reporting. For further information on Nature Portfolio policies, see our Editorial Policies and the Editorial Policy Checklist.

Statistics

For all statistical analyses, confirm that the following items are present in the figure legend, table legend, main text, or Methods section.

n/a	Confirmed	
☐	☒	The exact sample size (n) for each experimental group/condition, given as a discrete number and unit of measurement
☐	☒	A statement on whether measurements were taken from distinct samples or whether the same sample was measured repeatedly
☒	☐	The statistical test(s) used AND whether they are one- or two-sided *Only common tests should be described solely by name; describe more complex techniques in the Methods section.*
☒	☐	A description of all covariates tested
☒	☐	A description of any assumptions or corrections, such as tests of normality and adjustment for multiple comparisons
☐	☒	A full description of the statistical parameters including central tendency (e.g. means) or other basic estimates (e.g. regression coefficient) AND variation (e.g. standard deviation) or associated estimates of uncertainty (e.g. confidence intervals)
☒	☐	For null hypothesis testing, the test statistic (e.g. F, t, r) with confidence intervals, effect sizes, degrees of freedom and P value noted *Give P values as exact values whenever suitable.*
☒	☐	For Bayesian analysis, information on the choice of priors and Markov chain Monte Carlo settings
☒	☐	For hierarchical and complex designs, identification of the appropriate level for tests and full reporting of outcomes
☒	☐	Estimates of effect sizes (e.g. Cohen's d, Pearson's r), indicating how they were calculated

Our web collection on statistics for biologists contains articles on many of the points above.

Software and code

Policy information about availability of computer code

Data collection	Vienna ab initio simulation Package (VASP 5.4.1) was implemented under the Projector augmented wave (PAW) pseudopotentials for electrolyte simulations.
Data analysis	LAND V7.4, ZView 3.1, VESTA 3.5.7, CasaXPS 2.3.23, Origin V8.5, Topspin 4.1.3, and EC-lab V11.01

For manuscripts utilizing custom algorithms or software that are central to the research but not yet described in published literature, software must be made available to editors and reviewers. We strongly encourage code deposition in a community repository (e.g. GitHub). See the Nature Portfolio guidelines for submitting code & software for further information.

Data

Policy information about availability of data

All manuscripts must include a data availability statement. This statement should provide the following information, where applicable:
- Accession codes, unique identifiers, or web links for publicly available datasets
- A description of any restrictions on data availability
- For clinical datasets or third party data, please ensure that the statement adheres to our policy

The data that support the finding details of this study are available in Article and its Supplementary Information or from corresponding authors upon reasonable request.

Human research participants

Policy information about [studies involving human research participants and Sex and Gender in Research.](#)

Reporting on sex and gender	N/A
Population characteristics	N/A
Recruitment	N/A
Ethics oversight	N/A

Note that full information on the approval of the study protocol must also be provided in the manuscript.

Field-specific reporting

Please select the one below that is the best fit for your research. If you are not sure, read the appropriate sections before making your selection.

☐ Life sciences   ☐ Behavioural & social sciences   ☐ Ecological, evolutionary & environmental sciences

For a reference copy of the document with all sections, see [nature.com/documents/nr-reporting-summary-flat.pdf](#)

Life sciences study design

All studies must disclose on these points even when the disclosure is negative.

Sample size	Describe how sample size was determined, detailing any statistical methods used to predetermine sample size OR if no sample-size calculation was performed, describe how sample sizes were chosen and provide a rationale for why these sample sizes are sufficient.
Data exclusions	Describe any data exclusions. If no data were excluded from the analyses, state so OR if data were excluded, describe the exclusions and the rationale behind them, indicating whether exclusion criteria were pre-established.
Replication	Describe the measures taken to verify the reproducibility of the experimental findings. If all attempts at replication were successful, confirm this OR if there are any findings that were not replicated or cannot be reproduced, note this and describe why.
Randomization	Describe how samples/organisms/participants were allocated into experimental groups. If allocation was not random, describe how covariates were controlled OR if this is not relevant to your study, explain why.
Blinding	Describe whether the investigators were blinded to group allocation during data collection and/or analysis. If blinding was not possible, describe why OR explain why blinding was not relevant to your study.

Behavioural & social sciences study design

All studies must disclose on these points even when the disclosure is negative.

Study description	Briefly describe the study type including whether data are quantitative, qualitative, or mixed-methods (e.g. qualitative cross-sectional, quantitative experimental, mixed-methods case study).
Research sample	State the research sample (e.g. Harvard university undergraduates, villagers in rural India) and provide relevant demographic information (e.g. age, sex) and indicate whether the sample is representative. Provide a rationale for the study sample chosen. For studies involving existing datasets, please describe the dataset and source.
Sampling strategy	Describe the sampling procedure (e.g. random, snowball, stratified, convenience). Describe the statistical methods that were used to predetermine sample size OR if no sample-size calculation was performed, describe how sample sizes were chosen and provide a rationale for why these sample sizes are sufficient. For qualitative data, please indicate whether data saturation was considered, and what criteria were used to decide that no further sampling was needed.
Data collection	Provide details about the data collection procedure, including the instruments or devices used to record the data (e.g. pen and paper, computer, eye tracker, video or audio equipment) whether anyone was present besides the participant(s) and the researcher, and whether the researcher was blind to experimental condition and/or the study hypothesis during data collection.
Timing	Indicate the start and stop dates of data collection. If there is a gap between collection periods, state the dates for each sample cohort.

Data exclusions	*If no data were excluded from the analyses, state so OR if data were excluded, provide the exact number of exclusions and the rationale behind them, indicating whether exclusion criteria were pre-established.*
Non-participation	*State how many participants dropped out/declined participation and the reason(s) given OR provide response rate OR state that no participants dropped out/declined participation.*
Randomization	*If participants were not allocated into experimental groups, state so OR describe how participants were allocated to groups, and if allocation was not random, describe how covariates were controlled.*

Ecological, evolutionary & environmental sciences study design

All studies must disclose on these points even when the disclosure is negative.

Study description	*Briefly describe the study. For quantitative data include treatment factors and interactions, design structure (e.g. factorial, nested, hierarchical), nature and number of experimental units and replicates.*
Research sample	*Describe the research sample (e.g. a group of tagged Passer domesticus, all Stenocereus thurberi within Organ Pipe Cactus National Monument), and provide a rationale for the sample choice. When relevant, describe the organism taxa, source, sex, age range and any manipulations. State what population the sample is meant to represent when applicable. For studies involving existing datasets, describe the data and its source.*
Sampling strategy	*Note the sampling procedure. Describe the statistical methods that were used to predetermine sample size OR if no sample-size calculation was performed, describe how sample sizes were chosen and provide a rationale for why these sample sizes are sufficient.*
Data collection	*Describe the data collection procedure, including who recorded the data and how.*
Timing and spatial scale	*Indicate the start and stop dates of data collection, noting the frequency and periodicity of sampling and providing a rationale for these choices. If there is a gap between collection periods, state the dates for each sample cohort. Specify the spatial scale from which the data are taken*
Data exclusions	*If no data were excluded from the analyses, state so OR if data were excluded, describe the exclusions and the rationale behind them, indicating whether exclusion criteria were pre-established.*
Reproducibility	*Describe the measures taken to verify the reproducibility of experimental findings. For each experiment, note whether any attempts to repeat the experiment failed OR state that all attempts to repeat the experiment were successful.*
Randomization	*Describe how samples/organisms/participants were allocated into groups. If allocation was not random, describe how covariates were controlled. If this is not relevant to your study, explain why.*
Blinding	*Describe the extent of blinding used during data acquisition and analysis. If blinding was not possible, describe why OR explain why blinding was not relevant to your study.*

Did the study involve field work? ☐ Yes ☒ No

Reporting for specific materials, systems and methods

We require information from authors about some types of materials, experimental systems and methods used in many studies. Here, indicate whether each material, system or method listed is relevant to your study. If you are not sure if a list item applies to your research, read the appropriate section before selecting a response.

Materials & experimental systems

n/a	Involved in the study
☒	☐ Antibodies
☒	☐ Eukaryotic cell lines
☒	☐ Palaeontology and archaeology
☒	☐ Animals and other organisms
☒	☐ Clinical data
☒	☐ Dual use research of concern

Methods

n/a	Involved in the study
☒	☐ ChIP-seq
☒	☐ Flow cytometry
☒	☐ MRI-based neuroimaging